Finite-Temperature Machine-Learning Molecular Dynamics for Thermal Expansion and Structural Evolution in Perovskite Oxide Electrode Materials

Igor Evangelista,[1,*] Mathias A. Kiefer,[2] Liam A. V. Nagle-Cocco,[2] Michael J. Dzara,[3] Nicholas A. Strange,[2] Michal Bajdich,[1] and Kirsten T. Winther[1,†]

[1]*SUNCAT Center for Interface Science and Catalysis, SLAC National Accelerator Laboratory, 2575 Sand Hill Road, Menlo Park, California, 94025, USA*

[2]*Stanford Synchrotron Radiation Lightsource, SLAC National Accelerator Laboratory, Menlo Park, California, 94025, USA*

[3]*National Laboratory of the Rockies, Golden, Colorado, 80401, USA*

(Received 14 July 2026; revised 11 September 2026; accepted 25 September 2026; published 27 October 2026)

Thermal-expansion mismatch remains a major challenge for the long-term stability of solid oxide fuel-cell and electrolysis-cell materials, particularly for chemically complex perovskite electrodes operating at elevated temperatures. Reliable prediction of thermal expansion in these materials is difficult because anharmonic lattice dynamics, octahedral rotations, chemical disorder, and temperature-driven structural evolution can limit the applicability of conventional phonon-based approaches. Here, we combine quasiharmonic phonon calculations (QHA) and on-the-fly machine-learning force-field molecular dynamics (MLFF-MD) to evaluate finite-temperature structural behavior in $LaFeO_3$ and $La_{0.6}Sr_{0.4}Co_{0.2}Fe_{0.8}O_{3-\delta}$. $LaFeO_3$ was used as a benchmark material, and the QHA captures the qualitative expansion trend but overestimates the volumetric thermal expansion coefficient (TEC), giving $\alpha_V = 4.08 \times 10^{-5}$ K^{-1} compared with the high-temperature x-ray diffraction (HT-XRD) value of 3.52×10^{-5} K^{-1}. In contrast, MLFF-MD gives $\alpha_V = 3.56 \times 10^{-5}$ K^{-1}, in close agreement with the experiment. For $La_{0.6}Sr_{0.4}Co_{0.2}Fe_{0.8}O_{3-\delta}$, QHA becomes unreliable due to phonon instabilities, while MLFF-MD provides stable finite-temperature trajectories and captures the experimentally observed increase in linear TEC across the rhombohedral-to-cubic transition. Specifically, MLFF-MD predicts an increase in α_L from 1.31×10^{-5} K^{-1} in the low-temperature rhombohedral regime to 1.90×10^{-5} K^{-1} in the high-temperature cubic regime, consistent with the structural evolution observed experimentally. The remaining quantitative discrepancy with HT-XRD is consistent with the stoichiometric model used here, which isolates the intrinsic thermal expansion while excluding chemical-expansion contributions associated with oxygen nonstoichiometry under experimental conditions. Once trained, the MLFF reduces the cost of an individual molecular-dynamics step by roughly 2 orders of magnitude relative to direct *Ab Initio* molecular dynamics, enabling substantially longer trajectories and broader sampling of thermally accessible configurations while retaining close agreement with DFT reference energies and forces. These results show that on-the-fly MLFF-MD provides a practical first-principles framework for predicting thermal expansion and phase evolution in disordered solid-oxide perovskites beyond the regime where phonon-based QHA remains reliable.

DOI: 10.1103/xwd4-x84g

I. INTRODUCTION

The thermal expansion coefficient (TEC) plays a central role in the mechanical stability of solid-oxide electrolysis cells and solid-oxide fuel cells electrodes, where thermal-expansion mismatch between electrode and electrolyte layers can lead to interfacial stress accumulation, cracking, and long-term degradation [1–3]. As illustrated schematically in Fig. 1(a), perovskite oxygen electrodes such as $La_{0.6}Sr_{0.4}Co_{0.2}Fe_{0.8}O_{3-\delta}$ (LSCF) are integrated with dense electrolyte layers, such as yttria-stabilized zirconia (YSZ), in multilayer device architectures. Because these layers are mechanically coupled during heating, cooling, and high-temperature operation, differences in their thermal expansion can generate stresses at the electrode-electrolyte interface. The larger expansion of LSCF relative to YSZ can produce interfacial stress accumulation, cracking, delamination, and eventual

*Contact author: igord@stanford.edu
†Contact author: winther@slac.stanford.edu

Published by the American Physical Society under the terms of the Creative Commons Attribution 4.0 International license. Further distribution of this work must maintain attribution to the author(s) and the published article's title, journal citation, and DOI.

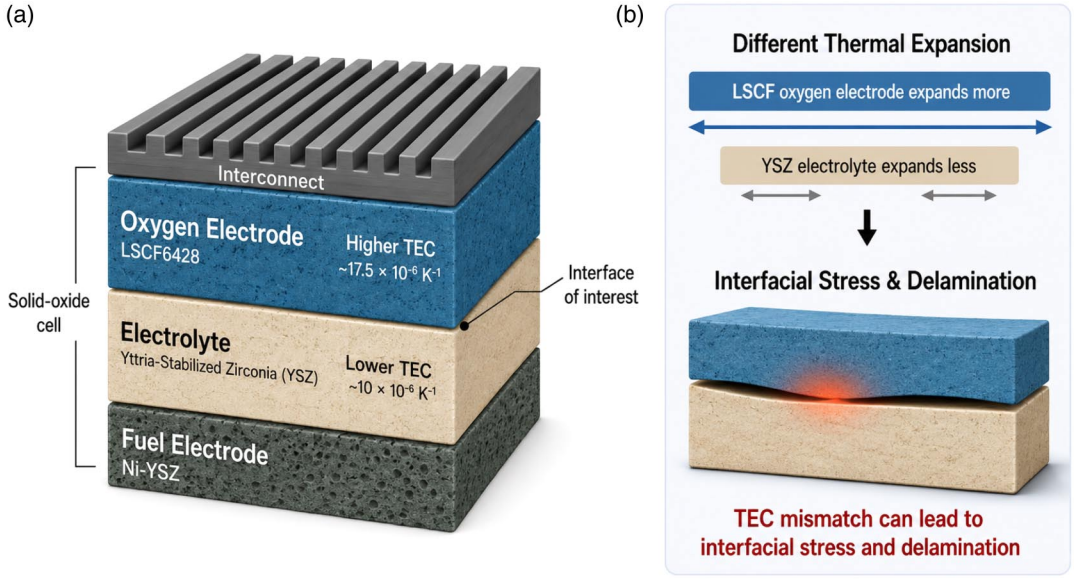


FIG. 1. Schematic illustration of thermal-expansion mismatch in a solid-oxide cell. (a) Simplified cross-sectional view of a single cell showing the interconnect, LSCF oxygen electrode, YSZ electrolyte, and Ni-YSZ fuel electrode. The larger TEC of LSCF relative to YSZ produces differential expansion during thermal cycling and high-temperature operation. (b) Schematic illustration of how this mismatch can generate interfacial stress and promote debonding or delamination at the oxygen electrode-electrolyte interface.

degradation of device functionality, as illustrated in Fig. 1(b). LSCF is a widely studied mixed ionic–electronic conducting perovskite electrode; however, its structural complexity, oxygen nonstoichiometry, and cation disorder make accurate prediction of temperature-dependent lattice behavior particularly challenging [4].

To place this challenge in quantitative context, the apparent linear TEC of LSCF measured in air is approximately $\alpha \approx 1.75 \times 10^{-5}\ \mathrm{K}^{-1}$ over the range 303–1273 K [5], while common electrolyte and interlayer materials generally exhibit lower TEC values. For example, yttria-stabilized zirconia (YSZ) has $\alpha \approx 1 \times 10^{-5}\ \mathrm{K}^{-1}$ [6], and gadolinium-doped ceriahas $\alpha \approx 12 \times 10^{-6}\ \mathrm{K}^{-1}$ [7]. Depending on the cell architecture and the presence of intermediate or cation-diffusion-barrier layers, the thermal-expansion mismatch between LSCF and adjacent cell components can contribute to thermomechanical stress at mechanically coupled interfaces during thermal cycling and high-temperature operation, potentially promoting interfacial damage or delamination [2,8]. This motivates accurate prediction of LSCF thermal expansion across the relevant operating temperature range.

The quasiharmonic approximation (QHA) is the conventional first-principles approach for calculating thermal expansion [9,10]. In QHA, phonon spectra are calculated at several volumes and used to construct a temperature-dependent free-energy surface, from which the equilibrium volume is obtained at each temperature. Although QHA provides accurate results for relatively simple crystalline solids, it treats lattice vibrations as harmonic at each fixed volume and includes anharmonicity only indirectly through the volume dependence of the phonon frequencies [11]. As such, QHA does not explicitly account for phonon-phonon interactions, temperature-dependent mode renormalization, or dynamic structural disorder. These effects become particularly important in complex oxides, where octahedral rotations, magnetic ordering, local chemical heterogeneity, and structural phase transitions can strongly couple to lattice dynamics and thermal expansion [12–15]. In perovskite oxygen electrodes such as LSCF, the application of QHA is further complicated by imaginary phonon modes and large supercell requirements [16]. These issues can prevent robust extraction of $\alpha(T)$ and motivate finite-temperature approaches capable of directly sampling anharmonic potential-energy surfaces.

Recent advances in machine-learned interatomic potentials (MLIPs) have enabled molecular dynamics simulations with near-first-principles accuracy at substantially reduced computational cost. Modern approaches include Gaussian approximation potentials, graph neural network potentials, and equivariant architectures such as NequIP, MACE, and related models, which have demonstrated high accuracy and data efficiency for atomistic simulations [17,18]. In this work, we use the on-the-fly machine-learned force-field formalism implemented in VASP, which combines molecular dynamics with Bayesian uncertainty estimation and automatic active learning of new DFT configurations during the simulation [19]. This integrated framework was chosen because it allows the force field to be generated consistently within the same DFT setup used for the reference calculations while

avoiding the need to construct a separate training database before running finite-temperature simulations. Similar active-learning MLIP strategies have been successfully applied to finite-temperature phase transitions in perovskites, demonstrating their ability to access length and timescales that are difficult for direct *ab initio* molecular dynamics [20]. More generally, the present results are not specific to a single MLIP architecture but demonstrate the advantage of well-validated machine-learned potentials for explicitly sampling finite-temperature lattice dynamics, anharmonicity, local structural fluctuations, and phase evolution under thermodynamic ensembles.

In this work, we systematically compare the QHA and on-the-fly machine-learning force-field molecular dynamics (MLFF-MD) for predicting finite-temperature thermal expansion in perovskite oxides of increasing chemical and structural complexity. In the MLFF-MD approach, the force field is iteratively updated during the simulation using selected density-functional theory calculations, enabling finite-temperature sampling beyond the harmonic phonon picture. We first benchmark both methods against high-temperature x-ray diffraction measurements for $LaFeO_3$, a stoichiometric orthorhombic perovskite with well-characterized thermal expansion. We then extend the analysis to $La_{0.6}Sr_{0.4}Co_{0.2}Fe_{0.8}O_{3-\delta}$ (LSCF), a technologically relevant mixed ionic–electronic conducting oxygen electrode material for solid oxide electrochemical devices. The broader goal of this work is therefore not only to compute the thermal expansion of a specific perovskite composition but also to establish a finite-temperature workflow for evaluating thermomechanical stability in complex oxide electrodes. By benchmarking against $LaFeO_3$ and then applying the approach to LSCF, we show how MLFF-MD can bridge the gap between atomistic modeling and experimentally relevant high-temperature structural behavior in energy materials.

II. METHODOLOGY

The computational workflow used to compare the QHA and MLFF-MD is summarized in Fig. 2. Figure 2(a) shows the QHA workflow, in which the structure is first relaxed using DFT, phonon spectra are then calculated at multiple strained volumes, and the resulting vibrational free energies are used to construct the temperature-dependent Helmholtz free-energy surface, $F(V,T)$. The equilibrium volume at each temperature is obtained by minimizing $F(V,T)$ with respect to volume, yielding $V(T)$ and the corresponding thermal-expansion coefficient. Figure 2(b) shows the on-the-fly active-learning MLFF-MD workflow. If no trained MLFF is available, an initial *ab initio* molecular dynamics trajectory is used to generate the force field. During subsequent MD, the MLFF predicts energies, forces, and stresses, while Bayesian uncertainty estimates are used to identify configurations that require explicit DFT evaluation. When the uncertainty exceeds the threshold, the configuration is added to the training set and the MLFF is updated. After the active-learning stage is complete, the trained MLFF is used in finite-temperature

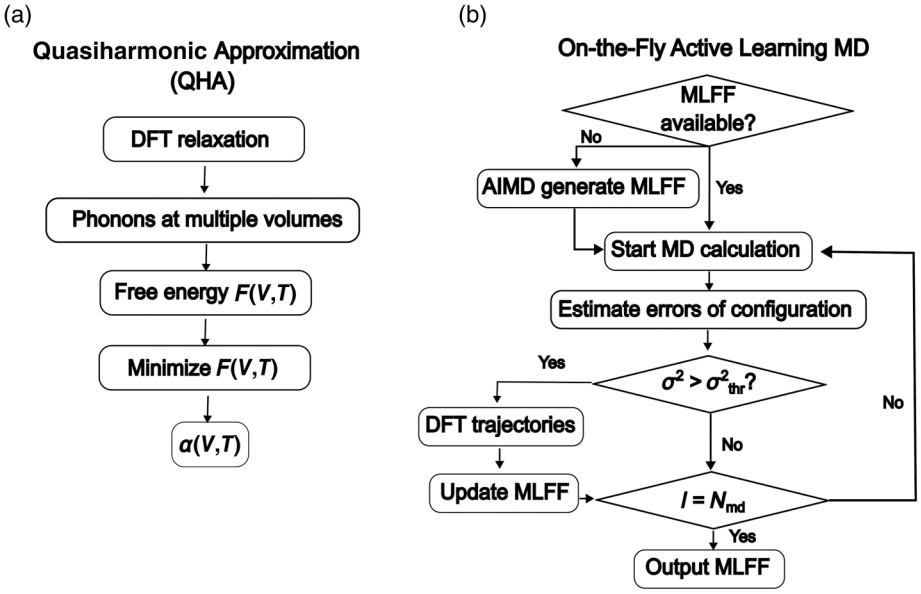


FIG. 2. Comparison of the QHA and active-learning MLFF-MD workflows for predicting temperature-dependent expansion. (a) In the QHA workflow, DFT-relaxed structures are used to calculate phonons at multiple volumes. These phonons are used to construct the temperature-dependent Helmholtz free energy, $F(V,T)$, and minimization of $F(V,T)$ gives the equilibrium volume path $V(T)$ and the thermal-expansion coefficient. (b) In the on-the-fly MLFF-MD workflow, the force field is iteratively updated during molecular dynamics when the Bayesian uncertainty exceeds the threshold σ^2_{thr}. The trained MLFF is then used in production NpT simulations to extract $V(T)$, thermal strain, and $\alpha(T)$ directly from finite-temperature trajectories.

NpT molecular dynamics simulations, from which $V(T)$, thermal strain, and $\alpha(T)$ are extracted directly from the resulting trajectories. The QHA calculations were performed using PHONOPY [9], while the finite-temperature molecular dynamics simulations used the on-the-fly MLFF formalism implemented in VASP [19].

A. First-principles calculations

All first-principles calculations were performed within density-functional theory (DFT) [21,22], as implemented in the Vienna *Ab initio* Simulation Package (VASP) [23,24]. The interaction between valence electrons and ionic cores was described using the projector augmented-wave method [25,26]. Exchange-correlation effects were treated within the generalized gradient approximation using the Perdew-Burke-Ernzerhof (PBE) functional, augmented with on-site Hubbard corrections (DFT + U) applied to transition-metal d states. Hubbard parameters of $U_{\mathrm{Fe}} = 4.3$ eV and $U_{\mathrm{Co}} = 3.32$ eV were used throughout this work, following established linear-response and oxide-formation-energy-based DFT + U parametrizations for localized transition-metal d states. [27,28]. The spin polarized calculations were carried out with high initial spin polarizations of Fe or Co ions. Brillouin zone integration was performed by means of Γ centered k-meshes having 2π Å^{-1} reciprocal space distance of 0.05. A plane-wave energy cutoff value of 520 eV was used in all calculations. Structural optimizations continued until convergence of atomic forces below 10^{-2} eV Å^{-1} was achieved. $LaFeO_3$ was considered in its orthorhombic *Pnma* phase with G-type antiferromagnetic ordering for the comparison of the QHA and MLFF-MD approach with experiments on high-temperature x-ray diffraction measurements. For LSCF, collinear spin-polarized DFT calculations were initialized with parallel moments of 5 μ_{B} on Fe and 3 μ_{B} on Co. Neither the total magnetization nor the site-resolved moments were constrained. The spin density was allowed to relax self-consistently whenever an explicit DFT reference evaluation was invoked during active learning. Analysis of these DFT-evaluated configurations showed that the Fe moments remained positive and close to 4 μ_{B} on average, whereas the Co moments were more configuration-dependent and sometimes became antiparallel to the Fe moments, particularly at higher temperatures. Disordered cation configurations were modeled using special quasirandom structures (SQS) generated with the ATAT package [29,30]. For LSCF, a 120-atom SQS supercell containing 24 perovskite formula units was used, with 14 La, 10 Sr, 19 Fe, 5 Co, and 72 O atoms. This corresponds to $La_{0.583}Sr_{0.417}Co_{0.208}Fe_{0.792}O_3$, which approximates the nominal $La_{0.6}Sr_{0.4}Co_{0.2}Fe_{0.8}O_3$ composition within finite-cell integer constraints. The oxygen sublattice was kept stoichiometric, corresponding to $\delta = 0$. The SQS was selected to reproduce the random A-site and B-site cation distributions as closely as possible within the finite supercell. The 120-atom cell was selected as a practical compromise between representing cation disorder, accommodating collective octahedral distortions, and maintaining the feasibility of the repeated DFT reference calculations required during MLFF construction. To assess the sensitivity of the LSCF results to the particular SQS realization, two additional 120-atom SQS cells with the same composition were generated and compared with the original SQS. First- and second-neighbor pair correlations for La/Sr, Fe/Co, and A-B cation pairs, together with MLFF-NpT simulations at 400, 900, and 1100 K, show that the predicted pseudocubic lattice parameter changes by at most 0.00357 Å across the tested SQS cells (Table S1 of Supplemental Material [31]).

B. Quasiharmonic approximation

Thermal expansion within the quasiharmonic approximation was obtained from volume-dependent phonon calculations. For each structure, a series of strained volumes was generated around the relaxed equilibrium volume, and phonon spectra were calculated at each volume using finite-displacement calculations with $2 \times 2 \times 2$ supercells of the relaxed orthorhombic unit cell. The Helmholtz free energy was constructed as

$$F(V,T) = E_0(V) + F_{\mathrm{vib}}(V,T). \tag{1}$$

Representative temperature-dependent free-energy curves and the corresponding equilibrium-volume path used to extract $V(T)$ are shown in Fig. S1 of Supplemental Material [31].

For LSCF, the QHA workflow was found to be unreliable because the selected magnetic and structural reference states exhibited imaginary phonon modes, as shown in the phonon density of states in Fig. S2 in Supplemental Material [31]. Since QHA requires dynamically stable harmonic phonon spectra over the relevant volume range, these instabilities prevent a robust construction of $F(V,T)$ and motivate the finite-temperature MLFF-MD approach.

C. On-the-fly MLFF molecular dynamics

The MLFF molecular dynamics simulations were performed within the on-the-fly active learning method that is incorporated into VASP code. During the training phase, the MLFF predicted energies, forces, and stresses at each molecular dynamics step, and VASP estimated the Bayesian uncertainties of the predicted forces. When this uncertainty exceeded the threshold value $\sigma^2 > \sigma^2_{\mathrm{thr}}$, the corresponding explicitly calculated configuration was included in the training set. In this way, the force field was updated continuously throughout the training stage. The MLFF for $LaFeO_3$ was trained using an NpT molecular dynamics simulation at 800 K. This elevated training temperature was chosen to sample a broader range of thermally accessible configurations, including

larger-amplitude octahedral distortions and anharmonic lattice fluctuations, thereby improving the transferability of the force field across the lower-temperature production simulations. In the case of LSCF, the NpT training simulations were carried out at 400 K based on the rhombohedral structure, 900 and 1100 K based on the cubic one. These temperatures were chosen to represent a low-temperature tilted structure and a high-temperature cubic-like structure associated with the rhombohedral-to-cubic transition. Once the force fields were obtained, production simulations were performed in a fully flexible-cell isothermal–isobaric (NpT) ensemble using a Langevin thermostat and Parrinello-Rahman barostat. Both the cell lengths and angles were allowed to evolve, permitting changes in cell volume and shape during the rhombohedral-to-cubic transition. Simulations were conducted from 300 to 1100 K in 100 K increments with a time step of 1 fs. At each temperature, 50 000 MD steps were performed, corresponding to 50 ps of simulation time. The first 10 000 steps at each temperature were discarded as equilibration, while the remaining 40 000 steps were used to compute average volumes, pseudocubic lattice parameters, and structural descriptors. Statistical uncertainties in the time-averaged pseudocubic lattice parameters were estimated using nonoverlapping 5 ps trajectory blocks. The average volume in each block was converted to a pseudocubic lattice parameter, and the standard error was calculated as the sample standard deviation of these block values divided by the square root of the number of blocks. The instantaneous cell-volume distributions were characterized separately using their sample standard deviations and are reported in Fig. S8 of Supplemental Material [31].

The MLFFs were constructed using standard radial and angular descriptors. The radial descriptor used a cutoff radius of 8.0 Å, a Gaussian width of 0.5 Å, and 12 radial basis functions. The angular descriptor used a cutoff radius of 5.0 Å, a Gaussian width of 0.5 Å, eight radial basis functions, and a maximum angular momentum of $l_{\max} = 3$. A fourth-order polynomial kernel was employed with a radial-descriptor weight of 0.1. Energies, forces, and stresses were assigned equal regression weights. For both materials, the initial Bayesian force-uncertainty threshold was 0.002 eV Å^{-1} and was updated automatically during on-the-fly training.

The final $LaFeO_3$ training database contained 139 DFT reference configurations and 2601 selected local atomic environments, comprising 623 La, 478 Fe, and 1500 O environments. The final combined LSCF database contained 626 DFT reference configurations and 6590 selected local atomic environments, comprising 867 La, 973 Sr, 955 Fe, 795 Co, and 3000 O environments. A DFT reference configuration corresponds to a complete atomic snapshot for which the energy, forces on all atoms, and stress tensor were calculated using DFT. The local reference environments are atomic neighborhoods selected from these DFT-labeled configurations for use as the MLFF basis and therefore do not represent additional DFT calculations.

The larger LSCF database reflects its broader chemical and configurational complexity. $LaFeO_3$ is an ordered three-element system sampled primarily within a single orthorhombic structural regime. In contrast, LSCF contains five elements, chemically disordered La/Sr and Fe/Co sublattices, and both low-temperature rhombohedral-like and high-temperature cubic-like configurations. Its training data therefore span a wider range of local chemical environments, octahedral distortions, lattice volumes, and thermally accessible structures. The database size itself was not used as a measure of MLFF accuracy. Predictive performance was evaluated separately using configurations excluded from training.

For analysis of octahedral tilt distributions in snapshots obtained from MLFF-MD, Python scripts utilizing PYMATGEN [32] analyzed all octahedra across time and space in the postequilibration trajectories, with time-sampling over 100 fs intervals to reduce autocorrelation. For each sampled configuration, B-sites (Fe or Co) were identified, and their nearest B-B neighbor vectors were used to define an orthonormal pseudocubic basis. The six nearest oxygen neighbors around each B-site were then assigned to ideal $\pm x$, $\pm y$, and $\pm z$ octahedral directions in this pseudocubic frame. A best-fit rigid rotation was obtained between the ideal and observed B-O direction sets, and the resulting rotation vector was decomposed into signed tilt components ϕ_x, ϕ_y, and ϕ_z. The distributions in Fig. 8 were obtained by pooling these signed per-octahedron tilt components over all sampled configurations and B-sites at each temperature, followed by histogram binning of the resulting angle populations.

D. Thermal expansion analysis

The thermal expansion was quantified using the normalized volumetric strain,

$$\varepsilon_V(T) = \frac{V(T) - V_0}{V_0}, \tag{2}$$

where V_0 is the reference volume at the lowest temperature considered. The volumetric thermal-expansion coefficient was obtained from linear fits to $\varepsilon_V(T)$,

$$\alpha_V \approx \frac{d\varepsilon_V}{dT}. \tag{3}$$

For LSCF, pseudocubic lattice parameters were calculated as

$$a_{\mathrm{pc}}(T) = \left(\frac{V(T)}{N_{\mathrm{f.u.}}}\right)^{1/3}, \tag{4}$$

where $N_{\text{f.u.}}$ is the number of formula units in the simulation cell. The linear thermal strain was then defined as

$$\varepsilon_L(T) = \frac{a_{\text{pc}}(T) - a_{\text{pc},0}}{a_{\text{pc},0}}, \tag{5}$$

and the linear thermal-expansion coefficient was obtained as

$$\alpha_L \approx \frac{d\varepsilon_L}{dT}. \tag{6}$$

E. Materials characterization

Variable-temperature x-ray diffraction measurements were used to determine the experimental temperature-dependent lattice parameters used for comparison with the computational predictions. Commercial LSCF powder (Fuel Cell Materials, High Grade Powder) was measured in its as-received state while $LaFeO_3$ was synthesized following the procedure reported by Gholam and Wang [33]. *In situ* powder x-ray diffraction measurements were performed at beamline 2-1 of the Stanford Synchrotron Radiation Lightsource (SSRL) in transmission geometry, using an incident wavelength of 0.729 Å. The absolute wavelength for the measurements was refined using an NIST 660 c LaB_6 standard. Angle-dispersive XRD data were acquired stepwise using a Pilatus 100 K area detector in portrait orientation. Two-dimensional diffraction images were normalized to the incident beam, stitched, and integrated into one-dimensional diffraction patterns using a Python script developed specifically for SSRL beamline 2-1. XRD measurements were performed using a capillary sample cell [34] equipped with Nichrome coil heaters. Powders were prepared in 1.0 mm outer diameter (o.d.) quartz capillaries (Hilgenberg) with a 0.01 mm wall thickness and an internally mounted type K thermocouple for regulating and measuring sample temperature. Measurements were performed in air between room temperature and 800 °C, with approximately 4 min equilibration times and temperature holds during data acquisition. Sequential Rietveld refinements were performed using TOPAS-Academic [35] to quantify structural evolution as a function of temperature. Refined parameters included lattice parameters, unit cell volumes, and phase fractions, enabling analysis of temperature-dependent phase transformations and structural changes.

III. RESULTS AND DISCUSSION

A. Structural description and model representation

To make the comparison between simple and complex perovskites, the structures of $LaFeO_3$ and LSCF are depicted in Fig. 3. $LaFeO_3$ crystallizes in an orthorhombic *Pnma* structure featuring cooperative octahedral tilts, whereas LSCF shows a temperature-induced structural transition starting from the rhombohedral $R\bar{3}c$ structure at low temperatures and reaching the averaged cubic $Pm\bar{3}m$ perovskite structure at higher temperatures. For LSCF calculations, the supercell was set up based on a pseudocubic approach. Even though the actual atomic configuration still reflects the octahedral tilt pattern of the rhombohedral structure, the lattice vectors of the simulation cell are set in a pseudocubic convention. The benefit of such treatment lies in the possibility of describing the lattice parameters in a similar manner to experiments using a pseudocubic picture. Most importantly, the pseudocubic approach can reflect a dynamic transition of the system between the rhombohedral structure and the cubic one during molecular dynamics runs. Specifically, as temperature increases, the average octahedral rotation amplitude decreases, and the long-range tilt order is progressively suppressed, leading to an effectively cubic average structure while local dynamic octahedral fluctuations remain present.

B. $LaFeO_3$ benchmark for thermal expansion

To establish a controlled baseline for evaluating first-principles approaches to thermal expansion, we first consider $LaFeO_3$, a prototypical orthorhombic perovskite

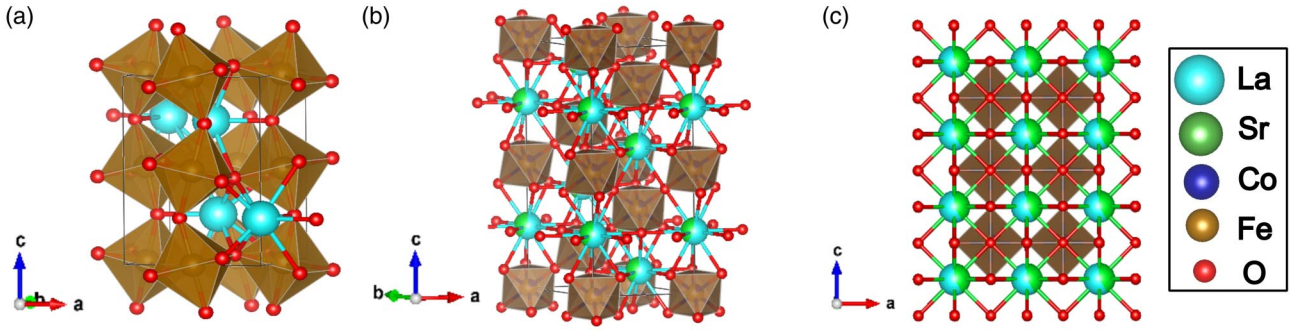


FIG. 3. Crystal structures considered in this work: (a) $LaFeO_3$ in the orthorhombic *Pnma* phase, (b) rhombohedral LSCF with $R\bar{3}c$ symmetry, and (c) ideal cubic LSCF with $Pm\bar{3}m$ symmetry. These structural models provide a basis for comparing the behavior of a stoichiometric tilted perovskite with the more complex temperature-dependent structural evolution of LSCF.

with well-characterized structural and thermophysical behavior. Its temperature-dependent crystal structure and thermal expansion have been studied using high-temperature x-ray diffraction and dilatometry, including reports of anisotropic expansion in the orthorhombic phase [36] and an orthorhombic-to-rhombohedral transition at elevated temperature [37]. In contrast to chemically complex oxygen-electrode materials such as LSCF, $LaFeO_3$ is stoichiometric and does not contain A-site disorder, mixed transition-metal chemistry, or significant oxygen nonstoichiometry. It therefore provides a useful reference system in which differences between QHA and MLFF-MD can be isolated without additional complications from chemical disorder.

The magnetic ground state of $LaFeO_3$ was determined by comparing the energies associated with different spin configurations. The spin configuration with lower energy is that corresponding to the G-type antiferromagnetic (AFM) order, which agrees with experimental data [38] and theoretical calculations reported earlier [39]. The G-type AFM ordering is energetically favored due to antiferromagnetic superexchange through Fe–O–Fe bonds in tilted-perovskite structure.

The optimized lattice parameters are $a = 5.57$ Å, $b = 7.91$ Å, and $c = 5.63$ Å. These values are in good agreement with experimental measurements reported in the literature. For example, Dixon *et al.* [40] report $a \approx 5.565$ Å, $b \approx 7.852$ Å, and $c \approx 5.555$ Å from powder neutron diffraction data at 275 K. The slight overestimation observed here is consistent with the known tendency of the PBE + U functional to overestimate lattice constants [41] and remains within approximately 1% of the experimental values.

From a crystallographic perspective, $LaFeO_3$ consists of a network of corner-sharing FeO_6 octahedra with cooperative $a^-b^+a^-$ tilts in Glazer notation. In tilted perovskites, thermal expansion is governed not only by bond dilation, but also by the temperature-dependent evolution of octahedral rotation modes [36,37]. These rotational modes are strongly anharmonic and couple directly to lattice strain, leading to anisotropic and temperature-dependent structural responses. As a result, $LaFeO_3$ provides an appropriate reference system for TEC calculations, because accurately reproducing its thermal expansion requires capturing both conventional vibrational expansion and anharmonic lattice dynamics associated with octahedral tilting.

Rietveld refinement of the variable-temperature HT-XRD data confirms that $LaFeO_3$ is well described by the orthorhombic *Pnma* structural model, as shown by the representative refinement in Fig. 4. Using the volumetric strain definition described in the Methodology section, the temperature-dependent expansion of $LaFeO_3$ was extracted from QHA, MLFF-MD, and HT-XRD data. The comparison was restricted to the 300–1000 K range to remain within the orthorhombic phase of $LaFeO_3$ and avoid the orthorhombic-to-rhombohedral phase transition reported to be at ~1228 K [36]. Rietveld refinement of the experimental HT-XRD measurements over the 300–1000 K range (Fig. S3 in Supplemental Material [31]) yields a volumetric thermal-expansion coefficient of $\alpha_V^{\mathrm{exp}} = 3.52 \times 10^{-5}$ K^{-1}, which serves as a quantitative reference for evaluating the computational predictions. This value is also consistent with reported pseudocubic thermal-expansion coefficients for orthorhombic $LaFeO_3$ [37].

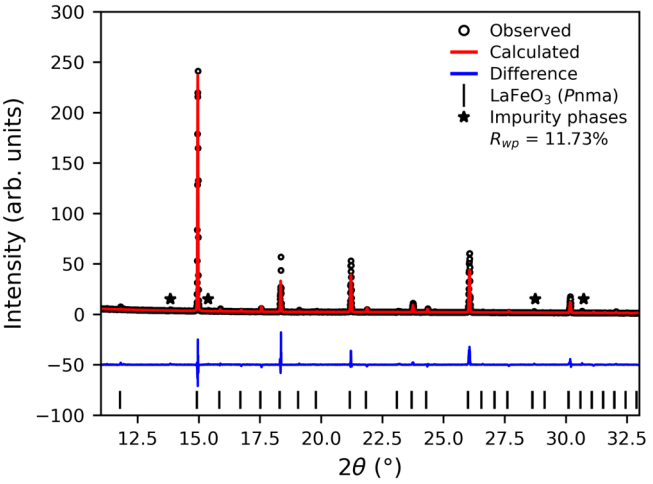


FIG. 4. Representative Rietveld refinement of $LaFeO_3$ from the variable-temperature x-ray diffraction dataset using the orthorhombic *Pnma* structural model.

The temperature-dependent volume expansion obtained from QHA, MLFF-MD, and HT-XRD is shown in Fig. 5. All three approaches follow the expected trend of increasing volume with temperature; however, quantitative and qualitative differences are evident from the slopes of the

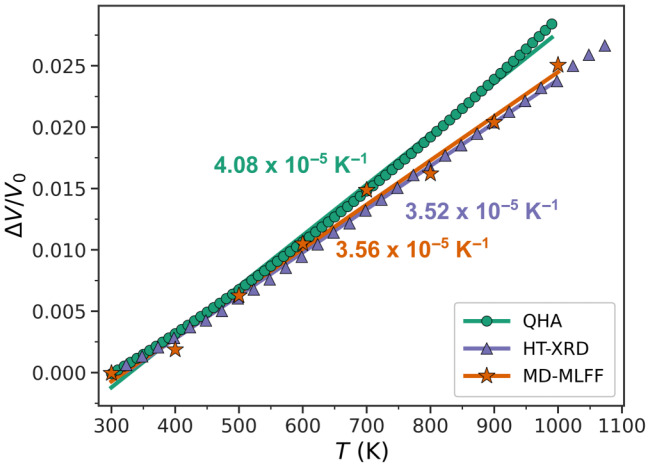


FIG. 5. Temperature-dependent volumetric strain of $LaFeO_3$ obtained from QHA,MLFF-MD, and high-temperature x-ray diffraction (HT-XRD). Lines indicate linear fits used to extract the volumetric thermal expansion coefficients.

curves. This allows $LaFeO_3$ to serve as a benchmark for thermal expansion within a single structural phase, rather than testing the ability of the methods to describe a phase transition. Within this temperature range, QHA predicts a volumetric thermal-expansion coefficient of $\alpha_V^{\mathrm{QHA}} = 4.08 \times 10^{-5}\ \mathrm{K}^{-1}$, corresponding to an overestimation of approximately 17% relative to the experimental HT-XRD value. This discrepancy becomes more pronounced above ~700 K, where the QHA curve shows a steeper temperature dependence than HT-XRD. Because solid-oxide cells operate at elevated temperatures, accurately capturing high-temperature lattice dynamics is essential for predicting thermomechanical behavior under realistic operating conditions.

In contrast, the TEC using MLFF-MD is $\alpha_V^{\mathrm{MLFF\text{-}MD}} = 3.56 \times 10^{-5}\ \mathrm{K}^{-1}$, in close agreement with the HT-XRD result. The MLFF-MD expansion curve follows the experimental trend across the full temperature range, capturing both the magnitude and temperature dependence of the volumetric strain. This behavior contrasts with QHA, which increasingly overestimates the expansion at higher temperature due to its steeper temperature dependence.

The origin of the QHA overestimation can be understood from several limitations of the approximation. Although QHA includes anharmonicity implicitly through the volume dependence of phonon frequencies, it does not explicitly account for phonon-phonon interactions, temperature-dependent mode renormalization, or dynamic fluctuations of octahedral rotation modes [11]. In orthorhombic perovskites such as $LaFeO_3$, these rotational modes are strongly coupled to lattice strain and can contribute substantially to the finite-temperature structural response. As temperature increases, dynamic fluctuations and mode-mode interactions can modify the effective lattice response in a way that is not fully captured by a static harmonic phonon description.

An additional limitation arises from the treatment of strain in the QHA workflow. In the present calculations, the equation of state was constructed by applying the same relative strain along all three lattice directions, corresponding to an isotropic volume-expansion path. However, orthorhombic $LaFeO_3$ exhibits anisotropic thermal expansion, with distinct expansion behavior along each crystallographic direction [37]. As a result, isotropic equation-of-state sampling can reproduce the overall volumetric expansion trend but does not fully capture the directional lattice response. This approximation may therefore contribute to the overestimation of the volumetric thermal-expansion coefficient obtained from QHA.

Additional contributions may also arise from magneto-structural coupling. $LaFeO_3$ is a G-type antiferromagnet at low temperatures, and coupling between magnetic order and lattice degrees of freedom can influence the equilibrium lattice parameters. Because the QHA calculations are performed using a fixed magnetic reference state, they do not capture temperature-dependent magnetic disorder or spin-lattice fluctuations, which may further contribute to deviations at elevated temperatures.

The reliability of the trained MLFF for $LaFeO_3$ was evaluated using an independent validation set. Specifically, 100 structures were randomly selected from a separate 400 K molecular dynamics trajectory that was not included in the training dataset. The corresponding MLFF-predicted energies and forces were compared with DFT reference calculations, as shown in Fig. S4 of Supplemental Material [31], yielding energy, force, and stress errors of 0.247 meV/atom and 0.0138 $\mathrm{eV/\AA}$, and 0.0290 GPa, respectively. This validation confirms that the trained force field accurately reproduces the DFT potential-energy surface for configurations outside the training set, supporting its use for finite-temperature production simulations.

By construction, MLFF-MD samples the finite-temperature potential-energy surface directly and allows the lattice to explore anharmonic configurations during the trajectory. This includes local structural distortions, dynamic fluctuations of octahedral tilts, and correlations between different vibrational modes. The close agreement between MLFF-MD and experiment therefore demonstrates that explicit finite-temperature sampling is important for quantitatively accurate prediction of thermal expansion in tilted perovskites.

Taken together, the $LaFeO_3$ benchmark establishes a clear methodological distinction. The QHA workflow required 27 method-specific DFT calculations, comprising 18 finite-displacement phonon calculations and nine strained-volume calculations, whereas MLFF training retained 139 DFT reference configurations. MLFF training therefore required 112 additional DFT evaluations or approximately 5.1 times the QHA count. Although QHA had a lower initial cost and captured the qualitative expansion trend, MLFF-MD yielded closer agreement with experiment, consistent with its direct sampling of finite-temperature anharmonic lattice dynamics. This capability is particularly important for LSCF, where mixed cation chemistry, oxygen nonstoichiometry, magnetic complexity, structural phase evolution, and imaginary phonon modes prevent reliable construction of the QHA free-energy surface.

C. Thermal expansion of LSCF

Having established the performance of both QHA and MLFF-MD in the controlled $LaFeO_3$ benchmark system, we now consider the technologically relevant mixed ionic–electronic conducting oxygen electrode material $La_{0.6}Sr_{0.4}Co_{0.2}Fe_{0.8}O_{3-\delta}$ (LSCF). In contrast to $LaFeO_3$, LSCF contains several simultaneous sources of structural and thermodynamic complexity, including mixed A-site and B-site chemistry, oxygen-vacancy disorder, and a temperature-driven rhombohedral-to-cubic

phase transition. These effects generate a strongly anharmonic free-energy landscape characterized by local distortions, fluctuating octahedral rotations, and substantial coupling between lattice, charge, and magnetic degrees of freedom.

Phonon calculations for LSCF reveal widespread imaginary frequencies, as shown in Fig. S2 in Supplemental Material [31], particularly within low-energy rotational branches associated with octahedral tilting distortions and local symmetry breaking. These imaginary modes indicate that the nominal reference structure is dynamically unstable within the harmonic approximation, preventing construction of a physically meaningful Helmholtz free-energy surface $F(V,T)$. As a result, equilibrium volumes and thermal-expansion coefficients derived from QHA become highly sensitive to the choice of magnetic ordering, structural representation, and supercell size. In practice, obtaining converged QHA predictions for LSCF would require extremely large disordered supercells and explicit averaging over multiple magnetic and configurational states, leading to computational costs that rapidly become prohibitive.

In contrast, MLFF-MD avoids the need for harmonic phonon expansions entirely by directly evolving atomic trajectories at finite temperature within the NpT ensemble. Because the machine-learned force field is iteratively refined during the simulation through on-the-fly active learning, the method remains robust across a wide range of local structural environments encountered during thermal evolution. This framework naturally incorporates anharmonic fluctuations, local distortions, thermal disorder, and phase evolution, enabling stable prediction of thermal expansion even in regimes where phonon-based approaches become not well defined. The accuracy of the trained LSCF MLFF was evaluated by comparing MLFF-predicted energies and forces with DFT reference calculations for low- and high-temperature configurations, as shown in Fig. S5 of Supplemental Material [31]. The validation gives an energy MAE of 3.15 meV/atom, force MAEs of 0.095–0.117 eV/Å, and stress components of 0.181 GPa supporting the use of the trained MLFF for finite-temperature production simulations.

Figure 6 compares the pseudocubic thermal expansion of LSCF from MLFF-MD with HT-XRD measurements. The error bars in Fig. 6 represent estimated block standard errors of the MLFF-MD averages. The corresponding instantaneous cell-volume distributions and sample standard deviations are provided in Fig. S8 of Supplemental Material [31]. The corresponding variable-temperature XRD heatmap is shown in Fig. S6 of Supplemental Material [31]. In the low-temperature (300–800 K) regime, LSCF comprises both cubic and rhombohedral phases (Fig. 7), where the expansion is relatively smaller than in the high-temperature cubic regime. This reduced expansion is associated with the tilted octahedral framework,

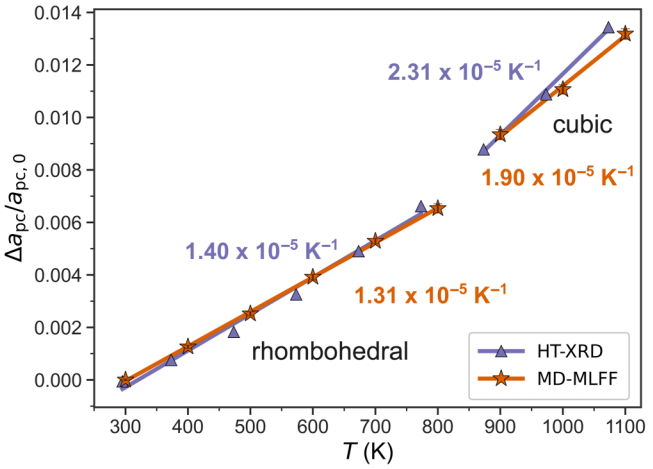


FIG. 6. Pseudocubic linear thermal strain of LSCF from MLFF-MD compared with HT-XRD. Separate linear fits are shown for the low-temperature rhombohedral regime and the high-temperature cubic regime. Error bars on the MD points represent estimated standard errors obtained from nonoverlapping 5 ps trajectory blocks.

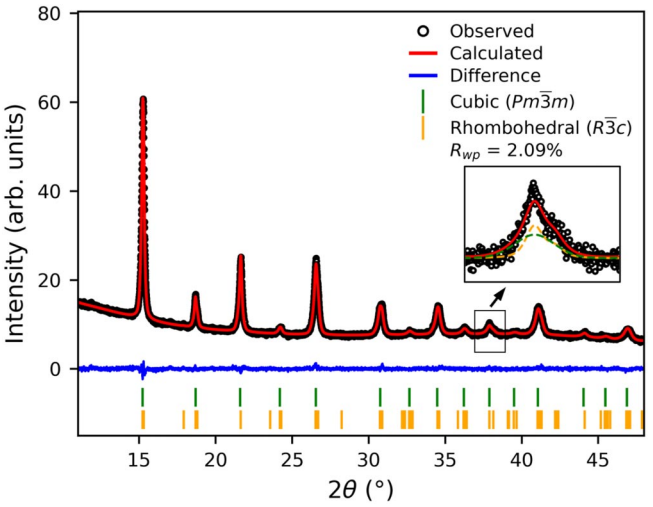


FIG. 7. Representative Rietveld refinement of LSCF from the variable-temperature x-ray diffraction dataset using the rhombohedral R-3c and cubic Pm-3m structural models. Subtle peak splitting from the mixed phase composition is shown in the inset.

which can accommodate part of the thermal strain through changes in octahedral rotations. Within this regime, MLFF-MD predicts a linear thermal-expansion coefficient of $\alpha_L^{\mathrm{MLFF}} \approx 1.31 \times 10^{-5}$ K^{-1}, in good agreement with the HT-XRD value of $\alpha_L^{\mathrm{HT\text{-}XRD}} \approx 1.40 \times 10^{-5}$ K^{-1}.

As the temperature increases toward the phase-transition region, the expansion becomes larger. This behavior is associated with the reduction of octahedral tilting. As the tilted rhombohedral framework is suppressed, the structure becomes less able to accommodate thermal strain through octahedral rotations, and lattice expansion becomes larger.

Above the transition region, LSCF evolves toward an average cubic structure with reduced rotational order and more isotropic thermal motion (Fig. S7 in Supplemental Material [31]). In this cubic regime (873–1100 K), MLFF-MD predicts a larger linear thermal-expansion coefficient of $\alpha_L^{\mathrm{MLFF}} \approx 1.90 \times 10^{-5}$ K^{-1}, compared with the HT-XRD value of $\alpha_L^{\text{HT-XRD}} \approx 2.31 \times 10^{-5}$ K^{-1}. The increase in α_L from the rhombohedral to cubic regime shows that the structural transition contributes directly to the enhanced high-temperature expansion of LSCF.

A key result is that the simulations reproduce the experimentally observed increase in thermal expansion across the structural transition without requiring explicit symmetry constraints or phase-specific parametrization. Instead, the transition emerges naturally from finite-temperature sampling of the anharmonic free-energy landscape. This is a key difference between MLFF-MD and standard phonon calculations. Rather than describing the system around a single static reference structure, MLFF-MD allows the lattice to evolve with temperature and sample both rhombohedral-like and cubic-like configurations.

The remaining quantitative discrepancy between MLFF-MD and HT-XRD in the high-temperature cubic regime is likely related to the absence of oxygen nonstoichiometry in the present simulations. The experimental HT-XRD measurements are conducted in air at elevated temperature, where LSCF can develop an oxygen deficit $\delta > 0$ through partial reduction of B-site cations, such as Fe^{4+}/Co^{3+} to Fe^{3+}/Co^{2+}. This fixed-stoichiometry approximation is expected to be most appropriate in the low-temperature rhombohedral regime, where reported oxygen deficiencies are small under oxidizing conditions, whereas thermally induced oxygen loss becomes more significant at higher temperature [4,42]. This reduction produces chemical expansion of the perovskite lattice because the reduced cations have larger ionic radii and oxygen-vacancy formation modifies the local electrostatic environment. As a result, the experimentally measured lattice expansion contains both intrinsic thermal-expansion and chemical-expansion contributions [14,15].

In contrast, the present MLFF-MD simulations model stoichiometric LSCF with fixed oxygen content ($\delta = 0$) over the full temperature range. Therefore, α_L^{MLFF} reflects primarily the intrinsic thermal component of the lattice response, while the additional chemical expansion contribution present in the HT-XRD measurements is absent by construction. Incorporating explicit oxygen vacancies in future MLFF-MD simulations, for example, through vacancy-seeded NpT trajectories with defect concentrations informed by experimental nonstoichiometry data, would allow the apparent thermal expansion under realistic operating conditions to be modeled more directly. Nevertheless, the overall agreement demonstrates that MLFF-MD captures the dominant structural mechanisms governing thermal expansion in LSCF, including the strong coupling between lattice strain and octahedral rotational dynamics.

D. Dynamics of phase transition and octahedral tilt

To further analyze the structural evolution captured during finite-temperature simulations, the distributions of octahedral tilt angles were evaluated as a function of temperature, as shown in Fig. 8. These distributions show how the octahedral tilts change with temperature across the rhombohedral-to-cubic transition, providing an atomic-scale view of the structural changes that contribute to thermal expansion. Because the high-temperature cubic phase is cubic in the time-averaged sense and instantaneous configurations retain thermally induced local distortions, these trajectory-averaged distributions provide a more representative structural descriptor than a single atomic snapshot.

At low temperatures, the tilt-angle distributions show distinct bimodal peaks at nonzero positive and negative rotational angles around 6°, consistent with the rhombohedral tilt system reported in crystallographic studies of LSCF [4,14,15]. These peaks correspond to cooperative octahedral rotations that stabilize the distorted perovskite framework through long-range rotational order, described in Glazer notation as $a^-a^-a^-$. The presence of well-defined nonzero rotor angles therefore indicates that the local structure sampled by MLFF-MD is consistent with the expected rhombohedral octahedral tilt pattern.

With increasing temperature, the distribution becomes broader and gradually shifts toward a peak near zero degrees. This evolution is already evident between 600 and 800 K and becomes more pronounced above 900 K. The effect is due to increasing thermal motion and the partial breakdown of the long-range octahedral tilting structure. As the structure approaches the cubic-like regime at high temperature, particularly above 900 K, the long-range octahedral tilt pattern is progressively suppressed. The average structure, therefore, becomes more symmetric, while local octahedral fluctuations remain dynamically active. Near the transition region, approximately over the 700–900 K range, the bimodal distributions begin to merge, indicating that the system is no longer confined to well-defined rhombohedral-like tilt configurations. The broad transition range observed in the simulations is consistent with experimental reports placing the rhombohedral-to-cubic transition in LSCF at approximately 923–1023 K, [43] supporting the interpretation that MLFF-MD captures the gradual loss of long-range tilt order across the transition.

At high temperatures, the distributions become increasingly centered on $\phi \approx 0°$. This closely matches the temperature range of the experimentally observed transition to a cubic average structure [43–46]. The consistency between local and average tilt order disappearance is significant,

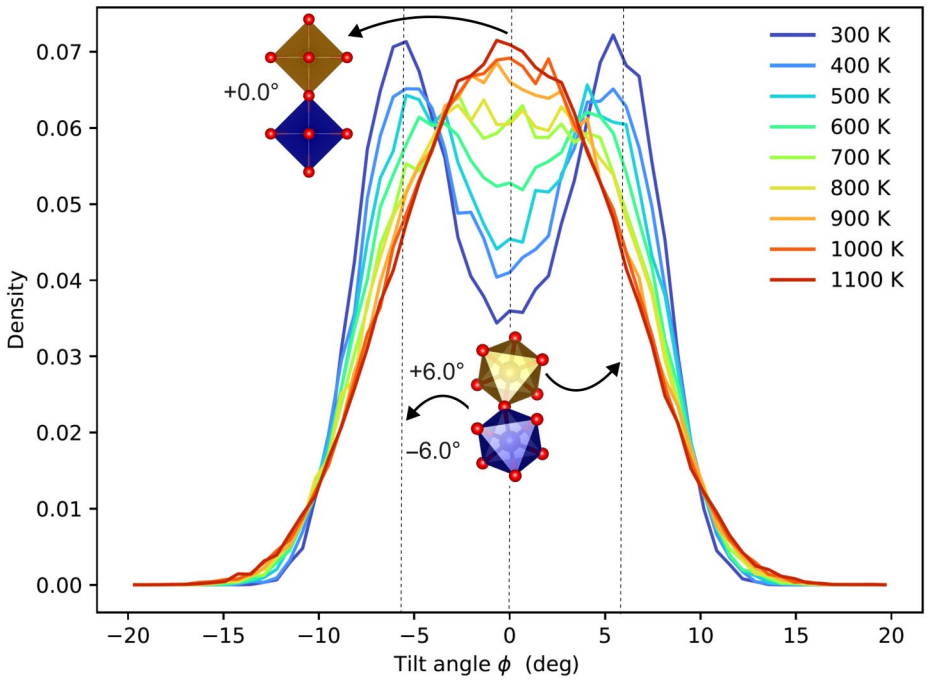


FIG. 8. Octahedral rotor-angle distributions of LSCF obtained from MLFF-MD as a function of temperature. The bimodal low-temperature distributions indicate rhombohedral octahedral tilting, while the progressive shift toward $\phi \approx 0°$ with increasing temperature reflects the rhombohedral-to-cubic structural evolution. The broad high-temperature distributions show that local octahedral fluctuations persist even in the average cubic regime.

indicating that the tilt order transition is at least partially displacive in character [12,47–49], though local fluctuations in the cubic phase may introduce some order-disorder character. Indeed, the tilt angle distribution closely resembles that obtained from total scattering analysis through the canonical tilt order transition in $SrTiO_3$ [48]. The observation of this transition in an O-stoichiometric system also indicates that the transition in LSCF-6428 is not attributable to oxygen vacancies.

A central result is that the phase transformation is obtained directly from unconstrained finite-temperature MLFF-MD simulations. No structural symmetry constraints, predefined order parameters, or externally imposed phase boundaries were introduced during the simulations. Instead, the changes in the rotor-angle distributions arise directly from the finite-temperature lattice dynamics sampled by MLFF-MD. This capability is particularly important for LSCF, where the structural response is governed by the interplay between octahedral tilting, local disorder, and lattice anharmonicity.

The ability of MLFF-MD to simultaneously capture thermal expansion and structural phase evolution demonstrates a major advantage over conventional quasiharmonic approaches. While QHA relies on static harmonic phonons around a reference structure, MLFF-MD directly resolves the temperature-dependent evolution of local lattice distortions and collective octahedral dynamics, providing a physically complete description of finite-temperature structural behavior in complex oxide materials.

IV. CONCLUSION

In this work, we have established a systematic comparison between the QHA and on-the-fly MLFF-MD for predicting thermal expansion in perovskite oxides of increasing complexity. For the benchmark system $LaFeO_3$, QHA captures the qualitative temperature dependence of thermal expansion but systematically overestimates the volumetric coefficient due to its neglect of explicit anharmonic effects. In contrast, MLFF-MD shows excellent agreement with experimental high-temperature x-ray diffraction measurements, demonstrating the importance of finite-temperature sampling.

In the case of LSCF, QHA becomes unreliable due to phonon instabilities, magnetic sensitivity, and chemical disorder. MLFF-MD, however, provides stable finite-temperature trajectories and captures the central experimental trend observed for LSCF, specifically the increase in linear thermal expansion as the system evolves from the low-temperature rhombohedral regime to the high-temperature cubic regime. This behavior is directly connected to the evolution of the octahedral framework. The low-temperature rotor-angle distributions show bimodal peaks associated with rhombohedral octahedral tilt order, whereas the high-temperature distributions broaden and shift toward zero angle, indicating the

progressive suppression of long-range rotational order and the emergence of an average cubic structure. These results show that the enhanced high-temperature expansion of LSCF is coupled to the loss of octahedral tilt order, rather than being only a simple increase in lattice parameter. Together, these results demonstrate that on-the-fly MLFF-MD provides a practical first-principles route for predicting thermomechanical behavior in chemically disordered oxide electrodes, particularly when anharmonicity, octahedral tilt dynamics, and structural phase evolution cannot be reliably captured by phonon-based QHA approaches.

Beyond its ability to capture finite-temperature anharmonicity and structural evolution, MLFF-MD also provides a substantial computational advantage over direct *ab initio* molecular dynamics. In the present calculations, a direct AIMD step required approximately 100 s, whereas an MLFF-evaluated step required approximately 0.4 s, corresponding to an acceleration of roughly 250× on a per-step basis. This reduction in computational cost enables substantially longer trajectories and broader configurational sampling while retaining close agreement with DFT reference energies and forces. Together, these results demonstrate that on-the-fly MLFF-MD provides a practical and computationally efficient first-principles framework for predicting thermomechanical behavior in chemically disordered oxide electrodes, particularly when anharmonicity, octahedral tilt dynamics, and structural phase evolution cannot be reliably captured by phonon-based QHA approaches or accessed efficiently using direct DFT-based molecular dynamics.

ACKNOWLEDGMENTS

This work was supported by the U.S. Department of Energy Office of Critical Minerals and Energy Innovation (CMEI), Alternative Fuels and Feedstocks Office (AFFO) under Contract No. DE-AC02-76SF00515 at SLAC National Accelerator Laboratory. This research used resources of the National Energy Research Scientific Computing Center (NERSC), a U.S. Department of Energy Office of Science User Facility supported by the Office of Science of the U.S. Department of Energy under Contract No. DE-AC02-05CH11231, through NERSC Award No. BES-ERCAP0037132. Use of the Stanford Synchrotron Radiation Lightsource (SSRL), SLAC National Accelerator Laboratory, was supported by the U.S. Department of Energy, Office of Science, Office of Basic Energy Sciences, under Contract No. DE-AC02-76SF00515. This work was authored in part by the National Laboratory of the Rockies for the U.S. Department of Energy (DOE), operated under Contract No. DE-AC36-08GO28308. The views expressed in this article do not necessarily represent the views of the U.S. Department of Energy or the U.S. Government. The U.S. Government retains and the publisher, by accepting the article for publication, acknowledges that the U.S. Government retains a nonexclusive, paid-up, irrevocable, worldwide license to publish or reproduce the published form of this work, or allow others to do so, for U.S. Government purposes.

DATA AVAILABILITY

The data supporting the findings of this study are available on Figshare at [50]. The dataset includes first-principles and machine-learned force-field (MLFF) data for $LaFeO_3$ and $La_{0.6}Sr_{0.4}Co_{0.2}Fe_{0.8}O_{3-\delta}$ (LSCF), organized into subfolders for QHA, density-functional perturbation theory (DFPT), MLFF training, MLFF production molecular dynamics, MLFF validation, and thermal-expansion analysis.

[1] Y. Gao, M. Zhang, M. Fu, W. Hu, H. Tong, and Z. Tao, *A comprehensive review of recent progresses in cathode materials for proton-conducting SOFCs*, Energy Rev. **2**, 100038 (2023).

[2] Y. Zhang, B. Chen, D. Guan, M. Xu, R. Ran, M. Ni, W. Zhou, R. O'Hayre, and Z. Shao, *Thermal-expansion offset for high-performance fuel cell cathodes*, Nature (London) **591**, 246 (2021).

[3] Y. Sun, D. Jin, X. Zhang, Q. Shao, C. Guan, R. Li, F. Cheng, X. Lin, G. Xiao, and J. Wang, *Controllable technology for thermal expansion coefficient of commercial materials for solid oxide electrolytic cells*, Materials **17**, 1216 (2024).

[4] L. Tai, *Structure and electrical properties of* $La_{1-x}Sr_xCo_{1-y}Fe_yO_3$. *Part 2. The system* $La_{1-x}Sr_xCo_{0.2}Fe_{0.8}O_3$, Solid State Ionics **76**, 273 (1995).

[5] H. Ullmann, N. Trofimenko, F. Tietz, D. Stöver, and A. Ahmad-Khanlou, *Correlation between thermal expansion and oxide ion transport in mixed conducting perovskite-type oxides for SOFC cathodes*, Solid State Ionics **138**, 79 (2000).

[6] F. Tietz, *Thermal expansion of SOFC materials*, Ionics **5**, 129 (1999).

[7] M. Mogensen, T. Lindegaard, U. R. Hansen, and G. Mogensen, *Physical properties of mixed conductor solid oxide fuel cell anodes of doped* CeO_2, J. Electrochem. Soc. **141**, 2122 (1994).

[8] N. Shah, X. Xu, J. Love, H. Wang, Z. Zhu, and L. Ge, *Mitigating thermal expansion effects in solid oxide fuel cell cathodes: A critical review*, J. Power Sources **599**, 234211 (2024).

[9] A. Togo and I. Tanaka, *First principles phonon calculations in materials science*, Scr. Mater. **108**, 1 (2015).

[10] E. T. Ritz, S. J. Li, and N. A. Benedek, *Thermal expansion in insulating solids from first principles*, J. Appl. Phys. **126**, 171102 (2019).

[11] P. B. Allen, *Theory of thermal expansion: Quasi-harmonic approximation and corrections from quasiparticle renormalization*, Mod. Phys. Lett. B **34**, 2050025 (2020).

[12] J. Klarbring and S. I. Simak, *Nature of the octahedral tilting phase transitions in perovskites: A case study of* $CaMnO_3$, Phys. Rev. B **97**, 024108 (2018).

[13] P. V. Balachandran and J. M. Rondinelli, *Interplay of octahedral rotations and breathing distortions in charge-ordering perovskite oxides*, Phys. Rev. B **88**, 054101 (2013).

[14] S.-I. Hashimoto, Y. Fukuda, M. Kuhn, K. Sato, K. Yashiro, and J. Mizusaki, *Thermal and chemical lattice expansibility of* $La_{0.6}Sr_{0.4}Co_{1-y}Fe_yO_{3-\delta}$ *(*$y = 0.2, 0.4, 0.6$ *and 0.8)*, Solid State Ionics **186**, 37 (2011).

[15] M. Kuhn, S. Hashimoto, K. Sato, K. Yashiro, and J. Mizusaki, *Thermo-chemical lattice expansion in* $La_{0.6}Sr_{0.4}Co_{1-y}Fe_yO_{3-\delta}$, Solid State Ionics **241**, 12 (2013).

[16] Z. Zhang and R. M. Wentzcovitch, *Ab initio anharmonic thermodynamic properties of cubic* $CaSiO_3$ *perovskite*, Phys. Rev. B **103**, 104108 (2021).

[17] S. Batzner, A. Musaelian, L. Sun, M. Geiger, J. P. Mailoa, M. Kornbluth, N. Molinari, T. E. Smidt, and B. Kozinsky, *E(3)-equivariant graph neural networks for data-efficient and accurate interatomic potentials*, Nat. Commun. **13**, 2453 (2022).

[18] I. Batatia, D. P. Kovács, G. N. C. Simm, C. Ortner, and G. Csányi, *MACE: Higher order equivariant message passing neural networks for fast and accurate force fields*, in *Advances in Neural Information Processing Systems* (Curran Associates, Inc., Red Hook, New York, 2022), Vol. 35, pp. 11423–11436, https://proceedings.neurips.cc/paper_files/paper/2022/hash/4a36c3c51af11ed9f34615b81edb5bbc-Abstract-Conference.html.

[19] R. Jinnouchi, F. Karsai, and G. Kresse, *On-the-fly machine learning force field generation: Application to melting points*, Phys. Rev. B **100**, 014105 (2019).

[20] R. Jinnouchi, J. Lahnsteiner, F. Karsai, G. Kresse, and M. Bokdam, *Phase transitions of hybrid perovskites simulated by machine-learning force fields trained on the fly with Bayesian inference*, Phys. Rev. Lett. **122**, 225701 (2019).

[21] P. Hohenberg and W. Kohn, *Inhomogeneous electron gas*, Phys. Rev. **136**, B864 (1964).

[22] W. Kohn and L. J. Sham, *Self-consistent equations including exchange and correlation effects*, Phys. Rev. **140**, A1133 (1965).

[23] G. Kresse and J. Furthmüller, *Efficient iterative schemes for ab initio total-energy calculations using a plane-wave basis set*, Phys. Rev. B **54**, 11169 (1996).

[24] G. Kresse and J. Furthmüller, *Efficiency of ab-initio total energy calculations for metals and semiconductors using a plane-wave basis set*, Comput. Mater. Sci. **6**, 15 (1996).

[25] P. E. Blöchl, *Projector augmented-wave method*, Phys. Rev. B **50**, 17953 (1994).

[26] G. Kresse and D. Joubert, *From ultrasoft pseudopotentials to the projector augmented-wave method*, Phys. Rev. B **59**, 1758 (1999).

[27] N. J. Mosey, P. Liao, and E. A. Carter, *Rotationally invariant ab initio evaluation of Coulomb and exchange parameters for* DFT + U *calculations*, J. Chem. Phys. **129**, 014103 (2008).

[28] A. Jain, G. Hautier, S. P. Ong, C. J. Moore, C. C. Fischer, K. A. Persson, and G. Ceder, *Formation enthalpies by mixing GGA and GGA + U calculations*, Phys. Rev. B **84**, 045115 (2011).

[29] A. Zunger, S.-H. Wei, L. G. Ferreira, and J. E. Bernard, *Special quasirandom structures*, Phys. Rev. Lett. **65**, 353 (1990).

[30] A. van de Walle, M. Asta, and G. Ceder, *The alloy theoretic automated toolkit: A user guide*, Calphad **26**, 539 (2002).

[31] See Supplemental Material at http://link.aps.org/supplemental/10.1103/xwd4-x84g for QHA free-energy curves, phonon density of states, variable-temperature x-ray diffraction data, MLFF validation, SQS comparisons, and simulation-cell volume distributions.

[32] S. P. Ong, W. D. Richards, A. Jain, G. Hautier, M. Kocher, S. Cholia, D. Gunter, V. L. Chevrier, K. A. Persson, and G. Ceder, *Python materials genomics (pymatgen): A robust, open-source python library for materials analysis*, Comput. Mater. Sci. **68**, 314 (2013).

[33] T. Gholam and H.-Q. Wang, *X-ray absorption spectroscopy study of iron site manganese substituted yttrium orthoferrite*, Molecules **27**, 7648 (2022).

[34] A. S. Hoffman, J. A. Singh, S. F. Bent, and S. R. Bare, *In situ observation of phase changes of a silica-supported cobalt catalyst for the Fischer–Tropsch process by the development of a synchrotron-compatible in situ/operando powder X-ray diffraction cell*, J. Synchrotron Radiat. **25**, 1673 (2018).

[35] A. A. Coelho, *TOPAS and TOPAS-academic: An optimization program integrating computer algebra and crystallographic objects written in* C + +, J. Appl. Crystallogr. **51**, 210 (2018).

[36] S. M. Selbach, J. R. Tolchard, A. Fossdal, and T. Grande, *Non-linear thermal evolution of the crystal structure and phase transitions of* $LaFeO_3$ *investigated by high-temperature x-ray diffraction*, J. Solid. State Chem. **196**, 249 (2012).

[37] A. Fossdal, M. Menon, I. Wærnhus, K. Wiik, M.-A. Einarsrud, and T. Grande, *Crystal structure and thermal expansion of* $La_{1-x}Sr_xFeO_{3-\delta}$ *materials*, J. Am. Ceram. Soc. **87**, 1952 (2004).

[38] T. Peterlin-Neumaier and E. Steichele, *Antiferromagnetic structure of* $LaFeO_3$ *from high-resolution tof neutron diffraction*, J. Magn. Magn. Mater. **59**, 351 (1986).

[39] Z. Mosleh and M. TarighiAhmadpour, *Impact of on-site and inter-site Coulomb interactions on the electronic, magnetic and thermomagnetic properties of* $LaFeO_3$*: Insights from* DFT + U *and* DFT + U + V, Results Phys. **78**, 108503 (2025).

[40] C. A. L. Dixon, C. M. Kavanagh, K. S. Knight, W. Kockelmann, F. D. Morrison, and P. Lightfoot, *Thermal evolution of the crystal structure of the orthorhombic perovskite* $LaFeO_3$, J. Solid State Chem. **230**, 337 (2015).

[41] G. I. Csonka, J. P. Perdew, A. Ruzsinszky, P. H. T. Philipsen, S. Lebègue, J. Paier, O. A. Vydrov, and J. G. Á ngyán, *Assessing the performance of recent density functionals for bulk solids*, Phys. Rev. B **79**, 155107 (2009).

[42] S.-I. Hashimoto, Y. Fukuda, M. Kuhn, K. Sato, K. Yashiro, and J. Mizusaki, *Oxygen nonstoichiometry and thermo-chemical stability of* $La_{0.6}Sr_{0.4}Co_{1-y}Fe_yO_{3-\delta}$ *(*$y = 0.2, 0.4, 0.6, 0.8$*)*, Solid State Ionics **181**, 1713 (2010).

[43] Y. Zou, M. Ziegner, J. Malzbender, and M. Krüger, *Investigation of rhombohedral-cubic phase transition of* $La_{0.58}Sr_{0.4}Co_{1-y}Fe_yO_{3-\delta}$ using high temperature XRD, Ceram. Int. **44**, 2822 (2018).

[44] J. N. Kuhn and U. S. Ozkan, *Effect of Co content upon the bulk structure of* Sr- *and* Co-*doped* $LaFeO_3$, Catal. Lett. **121**, 179 (2008).

[45] B. X. Huang, J. Malzbender, R. W. Steinbrech, E. Wessel, H. J. Penkalla, and L. Singheiser, *Mechanical aspects of ferro-elastic behavior and phase composition of* $La_{0.58}Sr_{0.4}Co_{1-y}Fe_yO_{3-\delta}$, J. Membr. Sci. **349**, 183 (2010).

[46] M. Daga, C. Sanna, G. Bais, M. Polentarutti, S. Massardo, M. Carnasciali, P. Holtappels, P. Costamagna, M. Pani, and C. Artini, *Impact of the electrospinning synthesis route on the structural and electrocatalytic features of the LSCF* $La_{0.6}Sr_{0.4}Co_{0.2}Fe_{0.8}O_{3-\delta}$, Solid State Ionics **413**, 116620 (2024).

[47] R. A. Cowley, *The phase transition of strontium titanate*, Philos. Trans. R. Soc., A, **354**, 2799 (1996).

[48] Q. Hui, M. G. Tucker, M. T. Dove, S. A. Wells, and D. A. Keen, *Total scattering and reverse Monte Carlo study of the 105 K displacive phase transition in strontium titanate*, J. Phys. Condens. Matter **17**, S111 (2005).

[49] A. B. S. Lavinscky, A.-M. Welsch, B. J. Kennedy, M. I. B. Bernardi, and V. R. Mastelaro, *Order-disorder phenomena and octahedral tilting in* $SrTi_{1-X}Sn_xO_3$ *perovskites—a structural and spectroscopic study*, J. Solid State Chem. **269**, 521 (2019).

[50] 10.6084/m9.figshare.32932712.